The Astrophysical Journal Letters, 970:L25 (7pp), 2024 August 1 https://doi.org/10.3847/2041-8213/ad5c5f

Constraining the Clustering and 21 cm Signature of Radio Galaxies at Cosmic Dawn

Sudipta Sikder[1], Rennan Barkana[1], and Anastasia Fialkov[2,3]
[1] School of Physics and Astronomy, Tel-Aviv University, Tel-Aviv, 69978, Israel; sudiptas@mail.tau.ac.il
[2] Institute of Astronomy, University of Cambridge, Madingley Road, Cambridge, CB3 0HA, UK
[3] Kavli Institute for Cosmology, Madingley Road, Cambridge, CB3 0HA, UK
Received 2024 January 4; revised 2024 May 27; accepted 2024 June 21; published 2024 July 22

Abstract

The efficiency of radio emission is an important unknown parameter of early galaxies at cosmic dawn, as models with high efficiency have been shown to modify the cosmological 21 cm signal substantially, deepening the absorption trough and boosting the 21 cm power spectrum. Such models have been previously directly constrained by the overall extragalactic radio background, as observed by Absolute Radiometer for Cosmology, Astrophysics, and Diffuse Emission 2 and Long Wavelength Array. In this work, we constrain the clustering of high-redshift radio sources by utilizing the observed upper limits on arcminute-scale anisotropy from the Very Large Array at 4.9 GHz and Australia Telescope Compact Array at 8.7 GHz. Using a seminumerical simulation of a plausible astrophysical model for illustration, we show that the clustering constraints on the radio efficiency are much stronger than those from the overall background intensity by a factor that varies between 18 and 55 in the redshift range of 7–22. As a result, the predicted maximum depth of the global 21 cm signal is lowered by a factor of 6 (to 1400 mK), and the maximum 21 cm power spectrum peak at cosmic dawn is lowered by a factor of 45 (to 1.3×10^5 mK^2). We conclude that the observed clustering is the strongest current direct constraint on such models, but strong early radio emission from galaxies remains viable for producing a strongly enhanced 21 cm signal from cosmic dawn.

Unified Astronomy Thesaurus concepts: Cosmology (343); H I line emission (690)

1. Introduction

The Absolute Radiometer for Cosmology, Astrophysics, and Diffuse Emission 2 (ARCADE-2) measurements of the absolute sky brightness at GHz frequencies provide evidence for a strong radio background that is consistent with the cosmic microwave background (CMB) radiation at higher frequencies. However, it significantly diverges from the blackbody spectrum at low frequency, as demonstrated by Fixsen et al. (2011). The result of ARCADE-2 was confirmed using the first station of the Long Wavelength Array (LWA-1; Dowell & Taylor 2018) in the frequency range 40–80 MHz. Since the amplitude of this radiation is considerably larger than anticipated based on observed radio counts of known galactic and extragalactic sources (Singal et al. 2018), the origin of this radio background is an interesting astrophysical mystery. While extragalactic explanations for the origins of this radio background suffer from various challenges (Singal et al. 2010; Kogut et al. 2011; Vernstrom et al. 2011; Condon et al. 2012; Vernstrom et al. 2014), previous works showed that the excess radio background could be produced by early radio-loud quasars (Bolgar et al. 2018), active galactic nuclei (AGN) from cosmic dawn (Ewall-Wice et al. 2014), the first generation of supermassive black holes (Biermann et al. 2014), or high-redshift star-forming galaxies (Condon 1992). It is important to remember that the Galactic contribution is uncertain (Subrahmanyan & Cowsik 2013), but the observed radio background certainly puts an upper limit on the contribution from any extragalactic source population.

After the reported EDGES measurement of an excess 21 cm absorption signal (Bowman et al. 2018), two classes of explanations were immediately offered for the anomalous EDGES absorption trough: an excess cooling of the ordinary matter through scattering with dark matter (Barkana 2018; Barkana et al. 2018, 2023; Berlin et al. 2018; Muñoz & Loeb 2018; Liu et al. 2019) and the enhancement of the CMB by an excess radio background, as explored in various works (Bowman et al. 2018; Feng & Holder 2018; Fialkov & Barkana 2019; Mirocha & Furlanetto 2019; Ewall-Wice et al. 2020; Mebane et al. 2020; Sikder et al. 2024). More recently, the SARAS-3 experiment (Singh et al. 2022) found a discrepancy between the EDGES absorption profile and their own measurements with a confidence level of 95%. Along with forthcoming findings from EDGES and SARAS, ongoing global signal experiments such as REACH (de Lera Acedo et al. 2022) and MIST (Monsalve et al. 2024) are poised to offer further insight into the observational quest for the global 21 cm signal.

The tentative EDGES signal and the extragalactic radio background measured by ARCADE-2 have served as a driving force for exploring astrophysically grounded excess radio models and analyzing their impact on the 21 cm signal. Reis et al. (2020) first incorporated a nonuniform radio excess from high-redshift galaxies into a 21 cm seminumerical code and investigated its effect on the global signal as well as on the 21 cm power spectrum. In our recent work (Sikder et al. 2024), we showed that a more accurate calculation of this radio excess, fully including the line-of-sight effect of individual radio galaxies, enhances the 21 cm power spectrum by up to 2 orders of magnitude during cosmic dawn (depending on the astrophysical parameters). In these papers, we considered the need not to overproduce the observed radio background and showed that the resulting constraint on the radio efficiency is

strongly redshift dependent, so that the efficiency could have been quite high at early times.

In this Letter, we consider observational constraints not just on the overall intensity of the cosmic radio background but also on its clustering. The most stringent constraints come from radio observations with the Very Large Array (VLA) at 4.9 GHz (Fomalont et al. 1988) and the Australia Telescope Compact Array (ATCA) at 8.7 GHz (Subrahmanyan et al. 2000). Holder (2014) pointed out that clustering is a strong constraint on low-redshift radio sources, and we consider much higher redshifts. Our seminumerical simulations of the early Universe allow us to predict the contribution of high-redshift galaxies to the observed clustering. Although the CMB dominates at these relatively high frequencies, even a population that makes a subdominant contribution can exceed the observed limits if that population is sufficiently strongly clustered. This can happen at high redshifts, when bright radio galaxies were rare and each served as a background source for strong 21 cm absorption. Using the existing upper limits, we aim to constrain the high-redshift radio clustering and investigate the consequences for the possible range of the cosmic dawn 21 cm signal.

2. Methodology

2.1. Astrophysical Model

To calculate the mean brightness temperature of the excess radio background at the redshifted wavelength of 21 cm radiation, as well as the 21 cm signal itself, we rely on our simulation code 21 cm Semi-numerical Predictions Across Cosmological Epochs, as detailed in previous works (see e.g., Visbal et al. 2012; Fialkov & Barkana 2014, 2019; Cohen et al. 2017). The simulation yields the 21 cm brightness temperature within a cosmological (comoving) volume of $[384\ \mathrm{Mpc}]^3$ at a resolution of 3 comoving Mpc, spanning a wide range of redshifts from 6 to 35. We focus on models with extra-strong radio emission from early galaxies, including the line-of-sight effect of individual radio galaxies (Reis et al. 2020; Sikder et al. 2024).

The basic simulated model has seven astrophysical parameters: star formation efficiency ($f_\star$), minimum mass of star-forming halos (given by a minimum circular velocity V_c, except that various types of feedback are also included), X-ray efficiency (f_X, where unity corresponds to the typical observed value for low-metallicity galaxies), X-ray spectral energy distribution (SED) parameters (power-law slope α and minimum X-ray energy E_min), and reionization parameters (ionization efficiency ζ and maximum mean free path of ionizing photons R_mfp). In addition, for models with strong radio emission we follow our previous papers and assume, based on the empirical relation of Gürkan et al. (2018), that the radio luminosity per unit frequency of a galaxy is proportional to its star formation rate and can be written as

$$L_\mathrm{Radio}(\nu, z) = f_\mathrm{Radio}\, 10^{22}\left(\frac{\nu}{150\ \mathrm{MHz}}\right)^{-\alpha_\mathrm{Radio}} \frac{\mathrm{SFR}}{M_\odot\ \mathrm{yr}^{-1}}, \quad (1)$$

where α_Radio is set to 0.7, as in Mirocha & Furlanetto (2019) and Gürkan et al. (2018). L_Radio is in units of $\mathrm{W\,Hz^{-1}}$. Here f_Radio represents the normalization of the radio emissivity, with $f_\mathrm{Radio} = 1$ being typical for the present-day star-forming galaxies. We also assume a radio spectral slope that corresponds to synchrotron radiation and roughly agrees with the slope of the observed extragalactic background.

2.2. Simulation Output

In order to obtain the radio observables from the simulation, we first note that the observed 21 cm brightness temperature relative to the CMB (in a pixel in some direction at redshift z) is

$$T_{21}^\mathrm{full} = \frac{(T_{R,\mathrm{los}} + T_\mathrm{CMB})e^{-\tau_{21}} + T_S(1 - e^{-\tau_{21}}) - T_\mathrm{CMB}}{1+z}. \quad (2)$$

Here $T_\mathrm{R,los}$ is the brightness temperature of the radio background from sources lying behind the pixel along our line of sight, T_S is the spin temperature, and τ_{21} is the 21 cm optical depth, where the latter two quantities depend on T_Radio, the isotropically averaged radio intensity at the relevant pixel (for details, see Sikder et al. 2024).

Consider the $\tau_{21} = 0$ limit of this expression:

$$T_{21}^{\tau=0}(z) = \frac{T_{R,\mathrm{los}}}{1+z}. \quad (3)$$

When there is no significant radio background (i.e., $T_{R,\mathrm{los}} \ll T_\mathrm{CMB}$), this $T_{21}^{\tau=0}$ term vanishes. Even when there is a radio background, the $\tau_{21} = 0$ term is normally subtracted (e.g., in our previous papers), since it represents a signal component that is independent of 21 cm emission or absorption (as it does not depend on τ_{21}), and has a spectrum that is similar to the Galactic synchrotron foreground. In 21 cm observations, this component cannot be distinguished from the Galactic synchrotron and is thus automatically removed when foreground removal is applied (under the assumption of a smooth power-law synchrotron spectrum), whether we are considering radio interferometers or global experiments. Here, however, we are interested in the total radio background, both its mean level and its clustering. The $T_{21}^{\tau=0}$ term strongly dominates the overall background, since τ_{21} is typically at the percent level.

Thus, we separate the 21 cm signal into two components. For the excess radio background at the redshifted wavelength of 21 cm radiation we adopt the $T_{21}^{\tau=0}$ term of Equation (3). On the other hand, when we consider standard 21 cm observations, the relevant (foreground subtracted) 21 cm brightness temperature is found by subtracting Equation (3) from Equation (2), which yields (Sikder et al. 2024)

$$T_{21}(z) = \frac{T_S - (T_{R,\mathrm{los}} + T_\mathrm{CMB})}{1+z}\,(1 - e^{-\tau_{21}}). \quad (4)$$

2.3. Mean Radio Background

Consider a particular astrophysical model with all the parameters of the high-redshift galaxies held fixed except that f_Radio is allowed to vary (and the total radio emission varies linearly with it). Based on the reported measurements of the extragalactic radio background at frequencies of 3, 8, and 10 GHz by ARCADE-2, the maximum possible radio background from unresolved sources can be written as follows (Holder 2014):

$$\langle T_{21}^{f_\mathrm{Radio}=1}(z)\rangle f_\mathrm{Radio}^\mathrm{mean}(z) = T_\mathrm{arcade} - T_\mathrm{counts}. \quad (5)$$

Here, on the right-hand side $T_\mathrm{arcade} = 28.3\ \mathrm{K}[\nu(z)/310]^{-2.6}$ is the observed extragalactic radio temperature (after adding twice

the error in order to get a 2σ upper limit); $T_{\rm counts} = 0.23\,{\rm K}[\nu(z)/1000]^{-2.7}$ is the expected temperature of the radio sky, based on extrapolating known source counts (Gervasi et al. 2008; Holder 2014); and $\nu(z) = 1420{\rm MHz}/(1+z)$. On the left-hand side, $\langle T_{21}^{f_{\rm Radio}=1}(z)\rangle$ is the mean (volume averaged) brightness temperature from the radio background at the redshifted wavelength of 21 cm radiation, $T_{21}^{\tau=0}$, in a simulation with $f_{\rm Radio} = 1$. Thus, $f_{\rm Radio}^{\rm mean}$ is the highest value of $f_{\rm Radio}$ (at each redshift) that is consistent with the observed upper limit on the mean extragalactic radio background.

2.4. Angular Power Spectrum

To calculate the angular power spectrum of the excess radio background at the redshifted wavelength of 21 cm radiation from our model, we use Equation (3) (since the $\tau_{21} = 0$ term dominates). Given the 3D brightness temperature cube at a redshift z, we choose a random slice to calculate the 2D power spectrum of radio fluctuations, $P_{\rm 2D}(k)$. We then use the power spectrum to find the squared fluctuation

$$\Delta^2(l) = \frac{1}{2\pi}\left(\frac{l}{R}\right)^2 P_{\rm 2D}(l/R)\ [{\rm mK}^2], \tag{6}$$

where the multipole number l is given by $l = kR$ and R is the distance (in Mpc) corresponding to the redshift z (where both k and R are comoving). Finally, we average this over all the slices of a particular simulation box at z and calculate the dimensionless (fractional) angular fluctuation

$$\frac{DT}{T} = \frac{\sqrt{\langle\Delta^2(l)\rangle}}{\langle T_{21}^{\tau=0}(z)\rangle}, \tag{7}$$

where $\langle T_{21}^{\tau=0}(z)\rangle$ is the mean brightness temperature of the simulation box at z.

We choose from Holder (2014) the two sets of observational data that are most constraining (quoting here 95% confidence limits): (a) an upper limit on DT/T of 1.4×10^{-5} at 8.7 GHz and $\theta = 120''$ (corresponding to $l = 4040$ using $l \sim 2.35/\theta$, as in Holder (2014)) from ATCA (Subrahmanyan et al. 2000) and (b) an upper limit on DT/T of 6×10^{-5} at 4.86 GHz and $\theta = 60''$ (corresponding to $l = 8080$) from the VLA (Fomalont et al. 1988). We calculate the dimensionless angular fluctuation (using Equation (7)) at $l_1 = 4040$ and $l_2 = 8080$ and refer to it henceforth as $\left(\frac{DT}{T}\right)_1$ and $\left(\frac{DT}{T}\right)_2$, respectively. Defined in this way, we note that this ratio is independent of $f_{\rm Radio}$, since both the numerator and denominator are proportional to this parameter.

To compare to observations of clustering, we need to account for the fact that the CMB also contributes to the radio background at these frequencies. For a given $f_{\rm Radio}$, at 8.7 GHz, the contribution of the high-redshift radio emission to the mean radio background is

$$[T_{21}^{\tau=0}(z)]_{8.7\ {\rm GHz}} = \langle T_{21}^{f_{\rm Radio}=1}(z)\rangle f_{\rm Radio}\left[\frac{8700}{\nu(z)}\right]^{-2.7}. \tag{8}$$

Since the CMB dominates at these frequencies, the upper limits on $f_{\rm Radio}$ due to clustering, corresponding to the measured upper limits on the angular power spectrum at l_1 and l_2, are as follows:

$$f_{\rm Radio}^{\rm DT1}(z) = \frac{1.4\times10^{-5}\times2.725}{\left(\frac{DT}{T}\right)_1\langle T_{21}^{f_{\rm Radio}=1}(z)\rangle\left[\frac{8700}{\nu(z)}\right]^{-2.7}}, \tag{9}$$

$$f_{\rm Radio}^{\rm DT2}(z) = \frac{6\times10^{-5}\times2.725}{\left(\frac{DT}{T}\right)_2\langle T_{21}^{f_{\rm Radio}=1}(z)\rangle\left[\frac{4860}{\nu(z)}\right]^{-2.7}}. \tag{10}$$

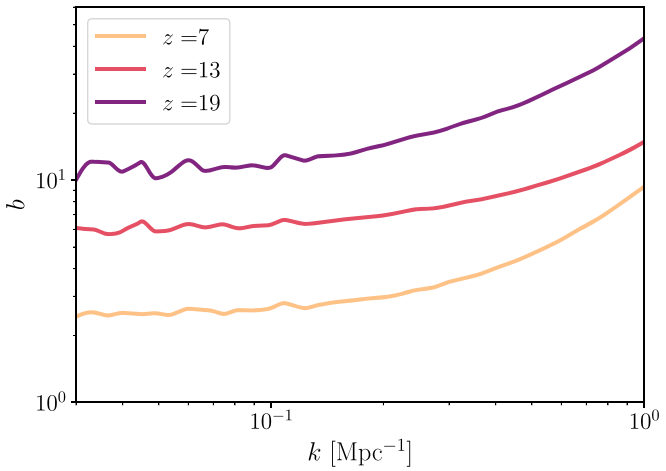

Figure 1. The bias b of gas in galactic halos shown as a function of wavenumber k at $z = 7$, 13, and 19.

3. Results

3.1. Bias of the Galaxy Population

Before considering the radio emission, we first consider the character of the underlying galaxy population, since its clustering ultimately drives that of the radio signal as well. Specifically, we find the bias factor

$$b = \frac{\Delta_{\rm g}}{\Delta_{\rm dm}}, \tag{11}$$

where $\Delta_{\rm dm}$ is the dimensionless fluctuation of dark matter (calculated from its power spectrum at each wavenumber k), and $\Delta_{\rm g}$ is the same but for the fraction of gas collapsed into galactic halos. Figure 1 illustrates the bias b as a function of wavenumber k at $z = 7$, 13, and 19 for our main model case. As expected, on large scales ($k \leqslant 0.1\ {\rm Mpc}^{-1}$), b is scale independent at each redshift. The large-scale bias increases with redshift up to $\sim$10 at $z = 19$, since the galaxies correspond to rare density peaks at early times. At each redshift, the bias increases on small scales and is enhanced by Poisson fluctuations (this figure shows the results from a single simulation run; see further discussion below). The substantial bias for the galaxy population contributes to the strong clustering signal that is predicted at high redshifts. We note that the $k = l/R$ values in this plot that correspond to the observational clustering constraints that we use in this Letter range over (e.g., at $z = 13$) 0.4–0.8 ${\rm Mpc}^{-1}$.

3.2. The Constraints from Radio Clustering

In order to study the constraints on high-redshift radio clustering, we choose a model (which we refer to as our main

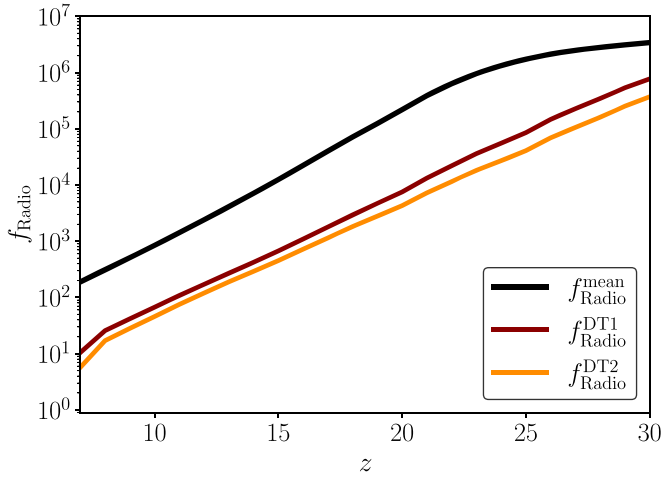

Figure 2. The radio efficiency $f_{\rm Radio}$ from our model as a function of z. We show (black line) the upper limit from the mean radio background ($f^{\rm mean}_{\rm Radio}$) as a function of z, i.e., the highest value that is consistent with the maximum possible radio background from unresolved sources as measured by ARCADE-2. We also show the maximum values that are consistent with the observed upper limit on clustering at 8.7 GHz from ATCA (dark red line) or at 4.86 GHz from the VLA (orange line). These results show the mean values from six simulation runs with independent random numbers, as there is some variation due to the combination of Poisson fluctuations and our limited box size. In the mean radio flux the variation is well below 1% at all redshifts, while in the clustering the variation is of order 1% except at the lowest redshift, where it is 30%, which yields an uncertainty in the sample mean $f^{\rm DT}_{\rm Radio}$ of 12%. The effect of Poisson fluctuations (compared to a simulation that assumes the mean halo mass function) is to lower $f^{\rm DT2}_{\rm Radio}$ by a factor of 3.33, 1.77, 1.35, 1.30, 1.54, and 1.92 at $z = 7$, 10, 13, 16, 19, and 22, respectively.

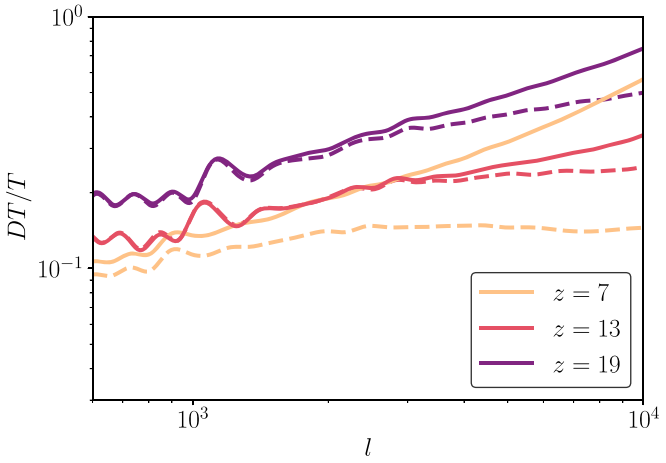

Figure 3. The predicted angular power spectrum (solid lines: with Poisson fluctuations, averaged over six simulation runs; dashed lines: without Poisson fluctuations) from high-redshift radio sources. We consider our main case at several redshifts ($z = 7$, 13, and 19). The quantity shown here is defined in Equation (7).

Table 1
Maximum $f_{\rm Radio}$ at Various Redshifts Corresponding to the Observed Upper Limits on the Mean Radio Background ($f^{\rm mean}_{\rm Radio}$) or on Fluctuations/Clustering in the Radio Background ($f^{\rm DT}_{\rm Radio}$)

Redshift	7	10	13	16	19	22
$f^{\rm DT}_{\rm Radio}$	5.70	45.8	189	722	2800	11,500
$f^{\rm mean}_{\rm Radio}$	189	843	4140	22,400	124,000	634,000

Note. The values correspond to the results shown in Figure 2. These numbers are the same for both of the astrophysical models that we consider in this Letter (i.e., they are independent of the X-ray efficiency).

case) where the seven astrophysical parameters are star formation efficiency $f_\star = 0.1$, $V_c = 16.5$ (corresponding to the minimum halo mass for star formation set by atomic cooling), a hard X-ray SED ($\alpha = 1.5$, $E_{\rm min} = 1$ keV) with an efficiency ($f_X = 1$) corresponding to the typical observed value for low-metallicity galaxies, an overall ionizing efficiency $\zeta = 11.4$, and a maximum mean free path of ionizing photons ($R_{\rm mfp}$) of 30 comoving Mpc. The constraints on $f_{\rm Radio}$ depend on $f_\star$ and V_c, plus some sensitivity at the low-redshift end (below $z \sim 10$) to the reionization parameters (reionization is more strongly constrained than other 21 cm parameters due to Planck, and the effect on radio emission from galaxies is due to photoheating feedback, which is significant only in the late stages of reionization, as discussed further below).

As explained in the previous section, we find the upper limits on the radio efficiency parameter $f_{\rm Radio}$ at each redshift, from the observed upper limits on the mean radio background ($f^{\rm mean}_{\rm Radio}$) and from each of the two upper limits on clustering ($f^{\rm DT1}_{\rm Radio}$ and $f^{\rm DT2}_{\rm Radio}$). These values are shown in Figure 2 as a function of z. The values of $f^{\rm DT1}_{\rm Radio}(z)$ and $f^{\rm DT2}_{\rm Radio}(z)$ are fairly similar, with $f^{\rm DT2}_{\rm Radio}(z)$ providing a slightly stricter limit than $f^{\rm DT1}_{\rm Radio}(z)$. We adopt the better limit (i.e., the lower of the two values) and refer to it as $f^{\rm DT}_{\rm Radio}(z)$. The values of $f^{\rm DT}_{\rm Radio}$ and $f^{\rm mean}_{\rm Radio}$ are also listed at various redshifts in Table 1.

Compared to the limit from the mean radio background ($f^{\rm mean}_{\rm Radio}$), which has been used in previous papers, the limit from clustering is lower (i.e., stronger) by around 1.5 orders of magnitude. More precisely, the relative factor by which the constraint improves is 33.1, 18.4, 21.9, 31.0, 44.3, and 55.1 at $z = 7$, 10, 13, 16, 19, and 22, respectively.

3.3. Predicted Angular Power Spectrum

Figure 3 shows the predicted angular power spectrum from high-redshift radio sources, for our main case, at several redshifts ($z = 7$, 13, and 19). The clustering increases strongly with redshift, reflecting the increased bias of galaxies along with the shot noise from the low number density of galaxies on the sky. We can roughly understand the limits on $f_{\rm Radio}$ as follows. For example, the observational constraint from the VLA is 6×10^{-5} at $l = 8080$ and 4.86 GHz, where DT/T at $z = 19$ (for example) is $\sim$0.645. This means that the $z = 19$ contribution to the radio background can only be a fraction of $6 \times 10^{-5}/0.645 \sim 9.3 \times 10^{-5}$. Now, if $f_{\rm Radio} = 3000$, we find from our simulation a mean 21 cm brightness temperature of 24.5 K from $z = 19$. The $z = 19$ 21 cm frequency (at which we calculate the output of the simulation) is 71 MHz, so given the synchrotron spectrum, at 4.86 GHz the contributed brightness temperature is $24.5\,{\rm K} \times (4860/71)^{-2.7} = 2.72 \times 10^{-4}$ K. This is 9.97×10^{-5} of the CMB (brightness) temperature, which dominates at this frequency. Since the fractional contribution, as noted above, can be up to 9.3×10^{-5}, this means that $f_{\rm Radio}$ can be up to 0.93 times 3000. The precise value we found in Table 1 is 2800.

3.4. Consequences for the 21 cm Signal

In this section we explore the consequences of the radio clustering constraints for the 21 cm signal. Here we use Equation (4), i.e., the $\tau_{21} = 0$ terms have been subtracted to

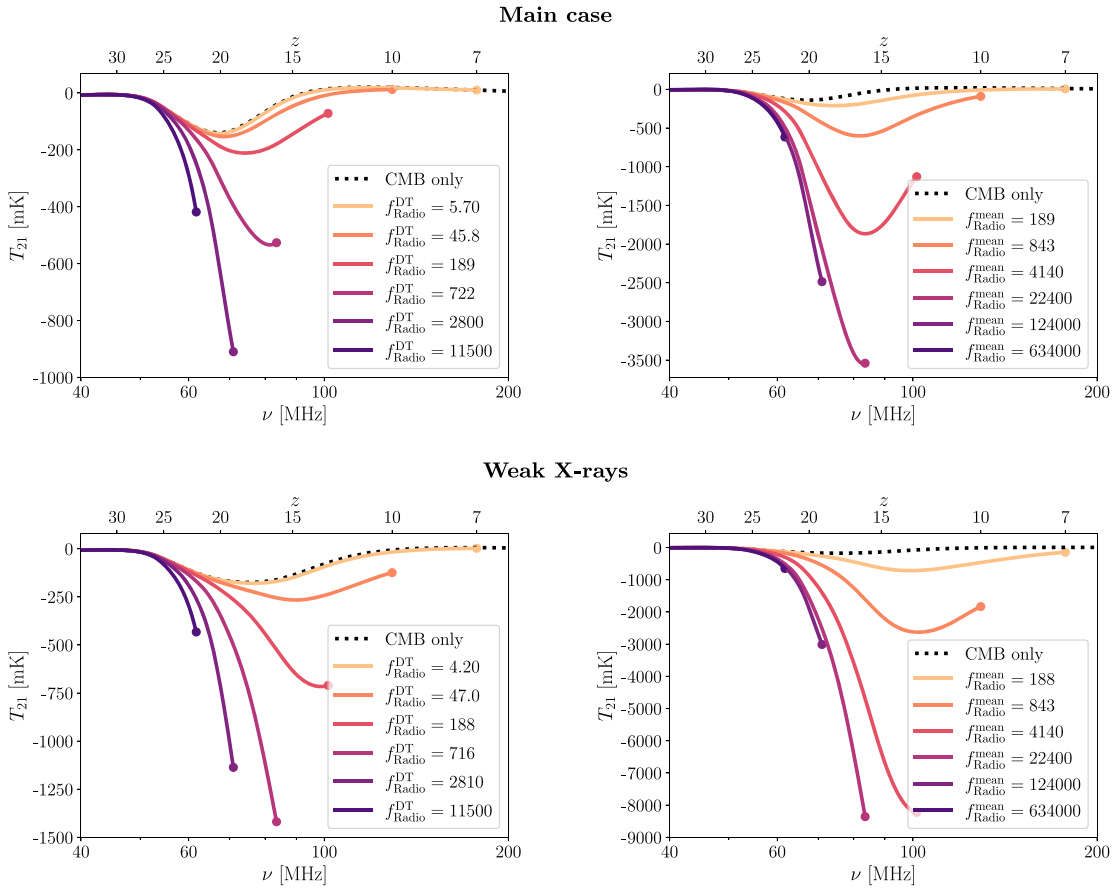

Figure 4. The global 21 cm signal from cosmic dawn as a function of ν (or z as the top x-axis) for various values of $f_{\rm Radio}$ from Table 1. Each curve is cut off at the redshift at which the radio emission corresponding to $f_{\rm Radio}$ (also listed in the legend) must be truncated in order not to overpredict the observed extragalactic radio background. We show the maximum model as constrained by radio fluctuations (left panels) or the mean background (right panels) for our main astrophysical model (top panels) or the model with a low X-ray efficiency (bottom panels). We also show the case with no excess radio background ($f_{\rm Radio} = 0$), i.e., the CMB-only case (dotted black line).

correspond to foreground removal in 21 cm observations (both global and interferometer based). We again show our results for our main astrophysical model ("main case"), as given in the previous subsection, which might represent a typical model. In order to have a better idea of the possible range of models, we also consider an additional model ("Weak X-rays"), in which the parameters are unchanged except that we assume a rather low X-ray efficiency, $f_{\rm X} = 0.01$. This substantially enhances the signal due to the weaker X-ray heating, since 21 cm absorption tends to give a stronger signal (both global and fluctuation) than 21 cm emission. Our experience with various model parameters suggests that this model represents something close to the maximum 21 cm signal at cosmic dawn. We comment further on the astrophysical parameters at the end of this subsection.

Figure 4 shows the maximum global 21 cm signal from cosmic dawn (and also the epoch of reionization) as a function of ν (or z as the top x-axis). Each curve shows the prediction of a particular model with a fixed $f_{\rm Radio}$, corresponding to one of the values in Table 1 (and also indicated in the legend). Note that the $f_{\rm Radio}$ constraints are sensitive only to galactic radio emission (i.e., the $\tau_{21} = 0$ terms) and are therefore independent of the X-ray efficiency. Each curve starts from high redshift and terminates at the particular redshift at which the radio emission associated with that $f_{\rm Radio}$ value is the maximum allowed by observations; thus, each curve shows the full redshift range over which that model is consistent with observations of the extragalactic radio background. The top panels show our main astrophysical model, while the bottom panels show the model with a low X-ray efficiency. The left panels show models corresponding to the constraint from the fluctuations/clumping of the radio background, while the right panels show the models as constrained only by the previously considered mean extragalactic radio background (note the very different y-axis ranges).

For the main case, the maximum absorption allowed by the mean radio background is -3550 mK (at $z = 16$), while including our new radio clustering constraint reduces this by a factor of 3.90 to just -910 mK (at $z = 19$). The weak X-ray model gives a significantly stronger global signal, down to -8360 mK (at $z = 16$) with only the mean background constraint and reduced by a factor of 5.89 to -1420 mK (at $z = 16$) with the clustering constraint. Thus, radio clustering is a much more important limit, but it still allows an absorption depth that can explain the EDGES detection and is more than 8 times larger than the same astrophysical model with no excess radio background (dotted black line). The clustering constraints are significantly stronger than the mean background constraint also at lower redshifts, though the relative factor decreases. At our lowest redshift, deep into the epoch of reionization, the difference again grows, since the combination of photoheating feedback (which shuts off star formation in small halos) with Poisson fluctuations produces a large fluctuation signal (as well as a significant variance in our results with various initial

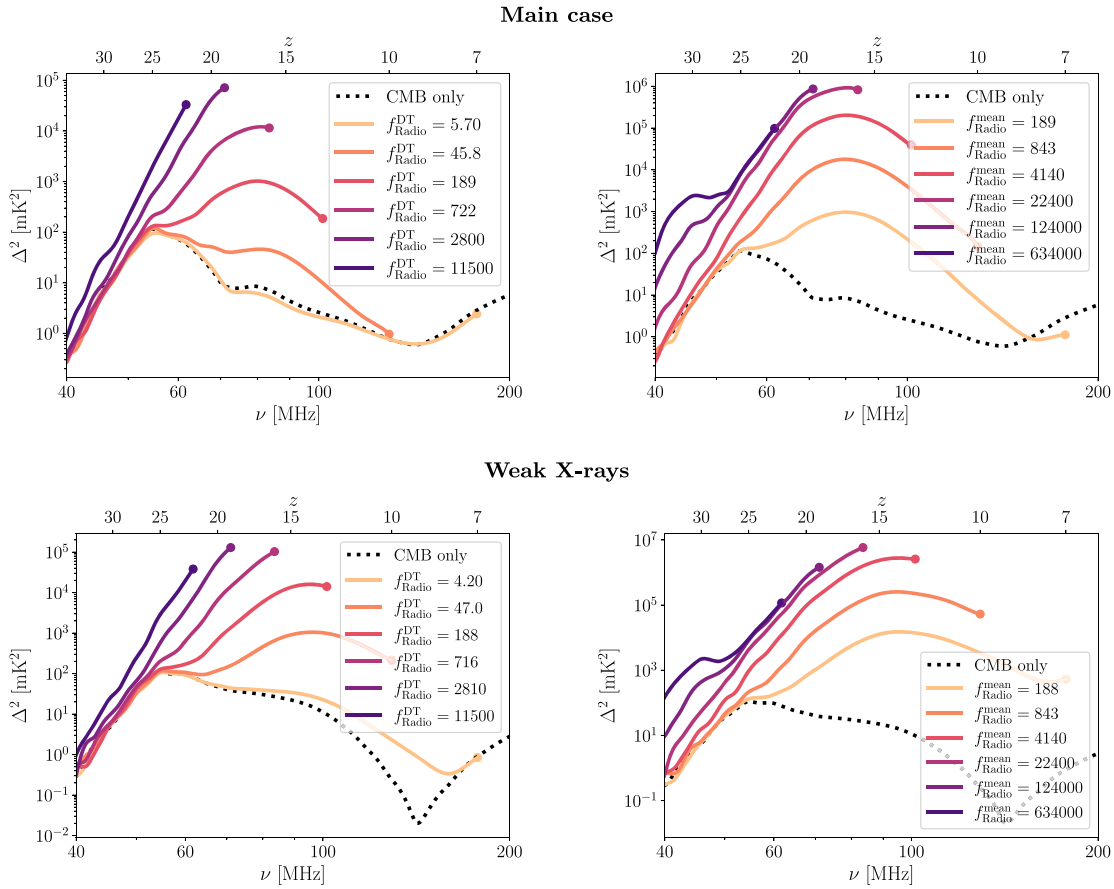

Figure 5. Same as Figure 4 except that here we show, instead of the global signal, the 21 cm power spectrum (in terms of the squared fluctuation) at $k = 0.1$ Mpc^{-1}.

conditions). This effect is not so noticeable in the standard 21 cm signal, since that fluctuation signal is dominated by the ionized bubbles (which arise from the contributions of many galaxies, integrated over time), but it is quite strong in the direct radio background fluctuations. We caution, though, that the $f_{\rm Radio}$ constraint from clustering during late reionization could be sensitive to the modeling of star formation during photoheating feedback, a complex astrophysical process that requires further study.

The other key observables in 21 cm cosmology are the statistical properties of the 21 cm fluctuations, usually quantified by the 21 cm power spectrum. The 21 cm power spectra as a function of ν (or z at the top x-axis) are shown in Figure 5. As in Figure 4, each curve shows a particular $f_{\rm Radio}$ value over the appropriate redshift range (and again, the y-axis ranges are quite different in the left and right panels). Specifically we show the squared fluctuation (in mK^2) at $k = 0.1$ Mpc^{-1}. For the main case, the maximum squared fluctuation allowed by the mean radio background is 9.26×10^5 mK^2 (at $z = 16.7$), while including the radio clustering constraint reduces this by a factor of 13 to just 7.15×10^4 mK^2 (at $z = 19$). As before, the weak X-ray model gives a significantly stronger signal of 5.85×10^6 mK^2 (at $z = 16$) with only the mean background constraint, reduced by a factor of 45 to 1.30×10^5 mK^2 (at $z = 19$) with the clustering constraint. Thus, the measured upper limits on radio fluctuations are significantly more constraining for the 21 cm power spectrum than the limits on the mean, overall radio background.

The factor by which the limit improves on the squared fluctuation is roughly the square of the factor of the improvement on the absorption depth of the global signal; this is not exact since the 21 cm fluctuations induced by the fluctuating high-redshift radio background compete with other sources of 21 cm fluctuations (density, Lyα coupling, X-ray heating, and reionization). Even with the reduced maximum 21 cm signal after inclusion of the radio clustering constraint, the 21 cm power spectrum at cosmic dawn redshifts (13–20) can still be up to four orders of magnitude larger than that expected from the same standard (CMB only) astrophysical scenario (dotted black line). This would increase by another order of magnitude if we only accounted for the observational constraint on the mean radio background. Since for a strong radio background, the main source of 21 cm fluctuations is initially radio fluctuations (plus those from Lyα coupling), lowering the X-ray efficiency does not affect much the 21 cm power spectrum at the highest redshifts, as can be seen from comparing the top and bottom panels of Figure 5 (the same is true in Figure 4, although this is harder to see due to the linear y-axis that is standard for the global signal). However, a low X-ray efficiency boosts the signal by up to 2 orders of magnitude compared to our main case at lower redshifts (<15) where heating fluctuations dominate.

We have illustrated the results for two particular sets of astrophysical parameters: a main case plus one with a rather low X-ray efficiency. While the particular constraints on $f_{\rm Radio}$ depend on the overall star formation history (as primarily determined by the parameters $f_\star$ and V_c), the resulting maximum 21 cm signal at each redshift should be less sensitive to these parameters, since the 21 cm signal and the overall radio emission tend to increase together as these parameters are

varied. The 21 cm signal at various redshifts does depend in a complex manner on the various astrophysical parameters, but for the range of possible signals at cosmic dawn redshifts, the main parameter is the X-ray efficiency, which we have significantly varied. The 21 cm power spectrum (as opposed to the global signal) is sensitive to additional parameters, e.g., a higher galactic halo mass (corresponding to a higher V_c) indicates rarer and more highly biased galaxies and thus yields stronger 21 cm fluctuations (after fixing the overall star formation rate by raising $f_\star$). In future work, we plan to explore the radio clustering constraints over the full range of possible radio-excess astrophysical models.

4. Summary and Discussion

We have explored new constraints on astrophysical models of high-redshift galaxies with a high efficiency of radio emission. Such models have been previously constrained by the overall extragalactic radio background as observed by ARCADE-2 and LWA-1, but we showed that a substantially stronger constraint comes from limiting the possible clustering of high-redshift radio sources due to the observed upper limits on arcminute-scale anisotropy from the VLA at 4.9 GHz and ATCA at 8.7 GHz. To illustrate this, we used a seminumerical simulation of a plausible astrophysical model for either a vanilla model or one with a particularly strong 21 cm signal achieved due to a low efficiency of X-ray production. We showed that the clustering constraints on the radio efficiency are stronger than those from the overall background intensity by a factor that varies between 18 and 55, generally increasing with redshift over the range $z = 7$–22. As a result, the predicted maximum depth of the global 21 cm signal is lowered by a factor of 5.89 (to -1419 mK) in the weak X-ray model and a factor of 3.90 (to -910 mK) in the vanilla model. The maximum 21 cm power spectrum peak at cosmic dawn is lowered by a factor of 45 (to 1.30×10^5 mK^2) in the weak X-ray model and a factor of 13 (to 7.15×10^4 mK^2) in the vanilla model.

We conclude that the observed clustering is currently the strongest direct constraint on such models, but strong early radio emission from galaxies remains viable for producing a strongly enhanced 21 cm signal from cosmic dawn. In particular, this can produce a global signal in the range of the possible EDGES detection, with an absorption depth that is 8 times larger than the same astrophysical model without a high radio efficiency. The corresponding 21 cm power spectrum peak during cosmic dawn is 3 orders of magnitude higher than for the same standard (CMB-only) model.

We note that in recent papers we and our collaborators have constrained excess radio models with current 21 cm data. Those constraints are more indirect than the radio background observations considered here, as the 21 cm signal is sensitive to various parameters and does not depend only on the radio emission from early galaxies. Also, in those papers the value of $f_{\rm Radio}$ was assumed to be fixed at all redshifts. In Bevins et al. (2024) we found a 1σ upper limit on $f_{\rm Radio}$ of 330, which is much weaker than the 2σ constraint we found here from clustering, especially given that Bevins et al. (2024) used data down to $z = 8$. In Pochinda et al. (2024), where we added the full radio line-of-sight fluctuations (as in the current Letter) and also Population III galaxies (which were not included here), the upper limit derived for $f_{\rm Radio}$ was 52 at 1σ and 5400 at 2σ. Thus, it is important to include the constraints from radio clustering when considering current and upcoming 21 cm experiments.

Acknowledgments

S.S. and R.B. acknowledge the support of the Israel Science Foundation (grant No. 2359/20).

Software: `Numpy` (Harris et al. 2020), `Scipy` (Virtanen et al. 2020), `matplotlib` (Hunter 2007).

ORCID iDs

Sudipta Sikder https://orcid.org/0000-0001-6129-0118
Rennan Barkana https://orcid.org/0000-0002-1557-693X
Anastasia Fialkov https://orcid.org/0000-0002-1369-633X

References

Barkana, R. 2018, Natur, 555, 71
Barkana, R., Fialkov, A., Liu, H., & Outmezguine, N. J. 2023, PhRvD, 108, 063503
Barkana, R., Outmezguine, N. J., Redigol, D., & Volansky, T. 2018, PhRvD, 98, 103005
Berlin, A., Hooper, D., Krnjaic, G., & McDermott, S. D. 2018, PhRvL, 121, 011102
Bevins, H. T. J., Heimersheim, S., Abril-Cabezas, I., et al. 2024, MNRAS, 527, 813
Biermann, P. L., Nath, B. B., Caramete, L. I., et al. 2014, MNRAS, 441, 1147
Bolgar, F., Eames, E., Hottier, C., & Semelin, B. 2018, MNRAS, 478, 5564
Bowman, J. D., Rogers, A. E. E., Monsalve, R. A., Mozdzen, T. J., & Mahesh, N. 2018, Natur, 555, 67
Cohen, A., Fialkov, A., Barkana, R., & Lotem, M. 2017, MNRAS, 472, 1915
Condon, J. J. 1992, ARA&A, 30, 575
Condon, J. J., Cotton, W. D., Fomalont, E. B., et al. 2012, ApJ, 758, 23
de Lera Acedo, E., de Villiers, D. I. L., Razavi-Ghods, N., et al. 2022, NatAs, 6, 1332
Dowell, J., & Taylor, G. B. 2018, ApJL, 858, L9
Ewall-Wice, A., Chang, T.-C., & Lazio, T. J. W. 2020, MNRAS, 492, 6086
Ewall-Wice, A., Dillon, J. S., Mesinger, A., & Hewitt, J. 2014, MNRAS, 441, 2476
Feng, C., & Holder, G. 2018, ApJL, 858, L17
Fialkov, A., & Barkana, R. 2014, MNRAS, 445, 213
Fialkov, A., & Barkana, R. 2019, MNRAS, 486, 1763
Fixsen, D. J., Kogut, A., Levin, S., et al. 2011, ApJ, 734, 5
Fomalont, E. B., Kellermann, K. I., Anderson, M. C., et al. 1988, AJ, 96, 1187
Gervasi, M., Tartari, A., Zannoni, M., Boella, G., & Sironi, G. 2008, ApJ, 682, 223
Gürkan, G., Hardcastle, M. J., Smith, D. J. B., et al. 2018, MNRAS, 475, 3010
Harris, C. R., Millman, K. J., van der Walt, S. J., et al. 2020, Natur, 585, 357
Holder, G. P. 2014, ApJ, 780, 112
Hunter, J. D. 2007, CSE, 9, 90
Kogut, A., Fixsen, D. J., Levin, S. M., et al. 2011, ApJ, 734, 4
Liu, H., Outmezguine, N. J., Redigolo, D., & Volansky, T. 2019, PhRvD, 100, 123011
Mebane, R. H., Mirocha, J., & Furlanetto, S. R. 2020, MNRAS, 493, 1217
Mirocha, J., & Furlanetto, S. R. 2019, MNRAS, 483, 1980
Monsalve, R. A., Altamirano, C., Bidula, V., et al. 2024, MNRAS, 530, 4125
Muñoz, J. B., & Loeb, A. 2018, arXiv:1802.10094
Pochinda, S., Gessey-Jones, T., Bevins, H. T. J., et al. 2024, MNRAS, 531, 1113
Reis, I., Fialkov, A., & Barkana, R. 2020, MNRAS, 499, 5993
Sikder, S., Barkana, R., Fialkov, A., & Reis, I. 2024, MNRAS, 527, 10975
Singal, J., Haider, J., Ajello, M., et al. 2018, PASP, 130, 036001
Singal, J., Stawarz, Ł., Lawrence, A., & Petrosian, V. 2010, MNRAS, 409, 1172
Singh, S., Jishnu, N. T., Subrahmanyan, R., et al. 2022, NatAs, 6, 607
Subrahmanyan, R., & Cowsik, R. 2013, ApJ, 776, 42
Subrahmanyan, R., Kesteven, M. J., Ekers, R. D., Sinclair, M., & Silk, J. 2000, MNRAS, 315, 808
Vernstrom, T., Scott, D., & Wall, J. V. 2011, MNRAS, 415, 3641
Vernstrom, T., Scott, D., Wall, J. V., et al. 2014, MNRAS, 440, 2791
Virtanen, P., Gommers, R., Oliphant, T. E., et al. 2020, NatMe, 17, 261
Visbal, E., Barkana, R., Fialkov, A., Tseliakhovich, D., & Hirata, C. M. 2012, Natur, 487, 70